PAPER

Check for updates

Pickering emulsions for stimuli-responsive transdermal drug delivery: effect of rheology and microstructure on performance†

Simona Migliozzi, [ID] *[a] Yiting He, [ID] [ab] Maryam Parhizkar, [ID] [c] Yang Lan [ID] [ab] and Panagiota Angeli [ID] *[a]

This work investigates the design of stimuli-responsive Pickering emulsions (PEs) for transdermal drug delivery applications, by exploring the impact of stabilising microgels size and interactions on their rheological and release properties. Temperature-responsive poly(N-isopropylacrylamide) microgels modified with 1-benzyl-3-vinylimidazolium bromide (pNIPAM-co-BVI) are synthesized in varying sizes and used to stabilise jojoba oil-in-water concentrated emulsions. The results reveals two distinct behaviours: for small microgels (~300 nm), the PEs exhibit a smooth, uniform structure characterised by a mild yield stress, characteristic of soft glassy systems. Conversely, larger microgels (~800 nm) induce droplet clustering, resulting in increased elasticity and a more complex yielding process. Interestingly, transdermal delivery tests demonstrate that microstructure, rather than bulk rheology, governs sustained drug release. The release process can be modelled as diffusion-controlled transport through a porous medium with random traps. At room temperature, the trap size corresponds to the droplet size, and the release time scales with the total dispersed phases volume fraction. However, at physiological temperature (37 °C), above the volume-phase transition temperature of the microgels, the release time increases significantly. The trap size approaches the microgel size, suggesting that microgel porosity becomes the dominant factor controlling drug release. Overall, the results highlight the critical role of microstructure design in optimising stimuli-responsive PEs for controlled transdermal drug delivery.

1 Introduction

In recent decades, the development of targeted drug delivery systems has received significant scientific and industrial interest. Traditional methods often require high dosages and frequent administrations, which can lead to poor patient compliance and severe side effects.[1] Significant efforts have been devoted towards designing and fabricating delivery systems that achieve greater specificity, improved stability of the

drugs, and controlled sustained release.[1–6] Among various delivery technologies, topical drug delivery through the skin (transdermal drug delivery) holds significant appeal due to several key benefits: (i) it offers an extended and controlled duration of therapeutic action, thereby reducing dosing frequency; (ii) it bypasses the gastrointestinal tract, minimising the impact on metabolism; and (iii) it can be non-invasive.[7–9]

In this context, optimal formulations should be semisolid, spreadable materials, ideally dosed with nanostructured microcarriers to allow localised drug transport to the diseased sites through the skin layers.[7,8,10,11] Pickering emulsions (PEs) are a promising strategy that combines these desired characteristics. PEs are surfactant-free dispersions of two phases, stabilised by nanoparticles absorbed at the interface. This approach offers the potential to create formulations with both the appropriate texture for topical application and the ability to deliver drugs.[8,12,13] By carefully engineering the stabilising nanoparticles, PEs offer design flexibility, where novel formulations with improved stability, specific rheological properties, increased shelf life and stimuli-responsive release functions can be tailored for a variety of different therapeutic applications, from

[a] *Department of Chemical Engineering, University College London, London, UK. E-mail: s.migliozzi@ucl.ac.uk, p.angeli@ucl.ac.uk*

[b] *Centre for Nature Inspired Engineering, University College London, London, UK*

[c] *School of Pharmacy, University College London, London, UK*

† Electronic supplementary information (ESI) available: (S1) Theoretical interfacial coverage of the Pickering droplets; (S2) drug release experiments; (S3) Pickering emulsions general aspect; (S4) zero-shear elastic plateau G_0' and yield stress σ_y as a function of microgel loading; (S5) calculation of the effective droplet volume fraction and of the total dispersed phases volume fraction; (S6) interfacial tension of the oil/microgel dispersions interface; (S7) additional graphs from strain amplitude sweep tests; (S8) small-amplitude oscillatory frequency sweeps. See DOI: https://doi.org/10.1039/d4sm00993b

transdermal delivery of drugs for the treatment of heart failure,[14] to injectable formulations for the release of hydrophobic drugs or biologics (*i.e.*, proteins, antibodies and enzymes).[15] In all these applications, ensuring the mechanical resistance of the microdroplets to applied stresses, and at the same time, optimal bulk functionality, is fundamental to preserve the drug stability and its sustained release.

To this aim, soft-crosslinked nanoparticles of hydrophilic polymers, known as microgels (MGs), emerge as promising interface stabilisers. Thanks to the rapid development of polymer particle synthesis techniques, MGs with desired properties and complex stimuli-responsive attributes can be designed for very targeted applications[16] as well as to address biocompatibility and toxicity issues often related to the use of common molecular surfactants.[17,18] Although several studies explored the use of novel microgel (MG)-stabilised Pickering emulsions in different bioapplications,[8,19,20] they primarily focused on the final performance and stability of specific oil and MG chemistry combinations. A gap remains in understanding the key physical attributes that influence the final properties of these formulations.

Microgels exhibit more intricate behaviour at interfaces compared to standard solid particles due to their unique dual particle/polymer nature. Similar to solid particles, MGs can irreversibly bind at interfaces. However, their polymeric structure allows them to stretch significantly along the interface plane.[21–23] The significant structural deformation, combined with the interpenetration of their polymer chains, controls MGs assembly at the interface, ultimately impacting the microstructure, stability and rheology of MG-stabilised PEs.[22–25] The ability of microgels to stretch and deform is, in turn, influenced by specific attributes, such as size, crosslinking degree and charge.[26–28] These properties can therefore be used as tuning parameters to design formulations with desired functionalities. For instance, larger MGs typically have a more uneven internal structure, which leads to a less uniform interfacial layer.[27] This less dense layer promotes bridging between neighbouring droplets, resulting in Pickering emulsions that are more prone to flocculation.[27] Conversely, smaller MGs stabilise more uniform and well-dispersed PEs due to their ability to create a denser and more uniform interfacial layer.[23,27] The degree of droplet aggregation significantly affects the rheology of the final emulsions.[29–32] This, in turn, is further influenced by other design parameters, such as the total volume fraction of oil droplets and the total amount of stabilising microgels added.[32–37] These factors complicate the design of PEs, especially for transdermal applications where smooth texture and good spreadability are essential. The microstructure formed by the assembly of all dispersed phases in the formulation also impacts its responsive behaviour. For instance, faster drug release is frequently observed when an external stimulus is applied to promote PEs destabilisation. This is usually attributed to the breakdown of the uniform external layer formed by the stabilising particles.[38,39] However, some studies have reported opposing trends for microgels-stabilised PEs,[40] highlighting the intricate interplay between microgel properties, the resulting microstructure, and the release kinetics of the encapsulated drug.

Hence, this study aims to elucidate the connection between the specific characteristics of responsive microgel particles and the overall performance of the resulting emulsions. In particular, we investigate how microgel size influences the microstructure and rheology of the resulting Pickering emulsions and explore how both aspects ultimately affect the final responsive drug release properties. To this end, we fabricated model Pickering emulsions stabilised with pNIPAM-based microgels of two distinct sizes. PNIPAM (poly(*N*-isopropylacrylamide)) microgels were chosen due to their well-established thermal responsiveness.[23,41] This responsiveness allows control over their swelling behaviour using temperature as external stimulus. Notably, pNIPAM undergoes a structural collapse at temperatures exceeding 32 °C.[42,43] This characteristic makes it an ideal candidate to investigate the performance of PEs stabilised by such microgels at physiological temperature (*i.e.*, 37 °C).

The general aspect and microstructural properties of the resulting PEs were analysed through bright-field and confocal microscopy, while strain amplitude oscillatory sweep measurements and time-resolved rheological analysis were performed to obtain a detailed characterisation of the PEs rheological properties and gain insights into the microstructure of the different formulations. Finally, the sustained release properties of the formulations were evaluated with the Franz-cell method[44,45] at both room and physiological temperatures, using levosimendan as a model lipophilic drug.[14] Through this multi-scale investigation, we wish to guide the design of PEs with tailored properties to achieve desired functionalities. By studying the material behaviour across a wide range of strain amplitudes, we aim to identify various microstructural rearrangements and gain insights into the underlying interactions. This approach provides valuable insights for designing these formulations from a physical perspective. This knowledge will be instrumental in optimising these systems for controlled drug delivery and other fields where controlled release is essential.

2 Materials and methods

2.1 Chemicals

N-Isopropylacrylamide (NIPAM), *N*,*N*′-methylenebis(acrylamide) (Bis), 2,2′-azobis(2-methyl-propionamidine)dihydrochloride (AIBA), benzyl bromide (BBr), 1-vinylimidazole (VImi), Rhodamine B isothiocyanate (RhodB), 2-aminoethyl methacrylate hydrochloride (AEMA-HC) and Nile Red were sourced from Sigma-Aldrich. Diethyl ether was from Acros Organics, cetyltrimethylammonium bromide (CTAB) was purchased from MP Biomedicals, LLC and Jojoba oil was supplied by Santa Cruz Biotechnology, Inc.

2.2 Microgels synthesis and characterisation

Monodisperse p(NIPAM-*co*-BVI) microgels (pNIPAM-*co*-BVI MGs), composed of monomer NIPAM and BVI, were synthesised in two different sizes through batch emulsion polymerization,[46]

following the same procedure reported in a previous work.[25] In brief, BVI was first synthesised as described by Liu *et al.*[47] Next, microgels with a swollen size $\sim$ 800 nm (M800) were fabricated by dissolving NIPAM (54.65 mmol), Bis (1.40 mmol) and BVI (0.86 mmol) in 298 mL DI water. The mixture was then purged with nitrogen for 20 minutes and 2 mL of AIBA (0.12 M) solution were injected into the flask to start the radical polymerization. The reaction was carried out at 70 °C and stirring speed of 700 rpm for 8 hours. To obtain microgels with smaller sizes, $\sim$ 300 nm (M300), 0.42 mmol CTAB were added to the initial mixture before purging. After polymerization, the microgels were purified with DI water by dialysis for one week, with DI water changed daily, and then concentrated with a rotavapor to obtain stock solutions at MG mass fractions higher than 8 wt%. To obtain fluorescently-tagged microgels for confocal imaging, 40 µL of 0.002 mM RhodB and AEMA–HC mixture (molar ratio 1 : 1) were added to the reaction mixture before heating. The characteristic sizes (d_p) and surface charge of the microgels synthesised as above were then determined using dynamic light scattering (DLS) and electrophoretic tests (Anton Paar Litesizer 100). For this purpose, 4 mL of 0.02 wt% solutions of M800 and M300 were prepared from the respective stock solutions and placed in a quartz cuvette. A temperature ramp (20 °C to 40 °C) was applied, and the temperature-dependent sizes and zeta-values (ζ) were measured at increments of 2.5 °C.

2.3 Emulsion preparation and characterisation

Pickering emulsions (PEs) were prepared with a fixed oil-to-water volume ratio of 1 : 1 through high shear homogenisation. Jojoba oil and microgel aqueous dispersions were emulsified using a high-shear mixer (Silverson, L5 series) at 10 000 rpm for 90 seconds. To investigate both the effect of microgel size and loading, for each of the two microgel sizes, three different microgel concentrations were tested, 6 wt% (C1), 4 wt% (C2), and 2 wt% (C3), for a total of six configurations.

2.3.1 **Microscopy techniques.** Bright-field microscopy and fluorescence microscopy (Zeiss Axio Observer 5 – Inverted microscope) were employed to characterise the droplet size distribution and emulsion type. Nile red, a fluorescent dye with an excitation wavelength of 565 nm, was incorporated into the oil phase to enhance visualisation. Diluted emulsion samples were deposited onto a gap created between two glass slides separated by cover slides to obtain clear microscopic images. In all cases, the emulsification process resulted in the formation of oil-in-water emulsions. The droplet size distribution for each sample was subsequently analysed using a custom MATLAB routine. The average droplet diameter (D_d) was determined by analysing at least 2000 droplets per sample, and calculated using the following equation:

$$D_d = \frac{\sum_i N_i D_i^3}{\sum_i N_i D_i^2} \tag{1}$$

where N_i is the total number of droplets with diameter D_i. Using the average droplet size, estimates of the theoretical interfacial coverage (C) of the emulsion droplets were obtained using a methodology applied in previous works.[27,48] Briefly, the total

surface area of the water-oil interface is first calculated as $S = 6V/D_d$, where V is the volume of jojoba oil used to fabricate the emulsion. Next, the equivalent area theoretically covered by microgel particles is determined using the equation $S_{eq} = n_p V \pi (d_p/2)^2$. Here, d_p is the hydrodynamic diameter of the microgels in their swollen state, and n_p represents the microgel number concentration, which is calculated using the rheological method described in Section 3.2. Finally, the interfacial coverage can be obtained as $C = S_{eq}/S$. The detailed results of this analysis are presented in Table S.1 of the ESI.†

To further observe the distribution of the microgels at the droplet interface, the PEs were also observed through confocal fluorescence microscopy (LSM 710 equipped with Plan-Apochromat 63×–40×/1.4 Oil DIC M27, Zeiss). Details of the sample preparation can be found in a previous publication.[25]

2.3.2 **Rheology measurements.** Rheological characterisation of all samples at room temperature (21 °C) was performed using an Anton Paar MCR302 rheometer equipped with a temperature-controlled Peltier plate and a parallel plate geometry (diameter: 40 mm) featuring sandblasted surfaces (roughness: 2 µm) to minimise slippage. A constant 1 mm gap size was maintained throughout the experiments. Prior to each test, samples underwent pre-shearing at a constant rate of 1 s^{-1} for 60 seconds followed by a 10 minute rest period. Note that rheological characterisation at physiological temperature (*i.e.*, 37 °C) is not feasible due to the heterogeneous phase separation of the PEs at this temperature, preventing meaningful bulk rheological measurements.

To investigate the influence of microgel size and loading on the microstructure of the material, strain amplitude oscillatory sweep tests were conducted. These measurements analyse the viscoelastic response of a material under small to large sinusoidal deformations, providing valuable insights into the physical mechanisms governing material yielding and, consequently, its microstructure. The tests were performed at a constant angular frequency (ω) of 10 rad s^{-1} and a variable strain amplitude (γ_0) ranging from 10^{-4} to 10^2. The choice of an angular frequency of 10 rad s^{-1} was primarily driven by technical considerations. Preliminary measurements revealed that lower frequencies (*e.g.*, 1 rad s^{-1}) introduced significant noise into the raw waveforms, especially for low-strain amplitudes and low viscoelasticity formulations (M300-C2/C3). To ensure data quality and enable reliable analysis, we opted for the higher frequency. While a different oscillating frequency could potentially explore distinct microstructural processes, we believe that the chosen frequency adequately samples the microstructure of our samples. The frequency-dependent viscoelastic moduli, obtained through small amplitude oscillatory sweeps for reference samples M300-C1/C3 and M80-C1/C3, are reported in the ESI† (S8). At each amplitude, the oscillations were maintained until a stable periodic signal was achieved. Subsequently, time-resolved data were collected over several oscillation periods. The acquired strain, shear rate, and stress waveforms were then analysed using the sequence of physical processes (SPP) approach. This technique, developed by Rogers,[49] offers a unique method for interpreting raw strain

amplitude oscillatory sweep data, revealing the underlying physical processes responsible for yielding behaviour.[50–55] All data processing was performed using the MATLAB-based SPPplus v2 software[53] (kindly provided by Prof. Rogers). The software first employs Fourier-domain filtering to reconstruct the data, utilising all detectable odd harmonics, then applies the SPP framework, which will be further discussed in the following section.

2.3.3 Fourier-transform decomposition and SPP analysis. When performing a strain amplitude oscillatory test, the stress response of a sample is tested under a sinusoidal strain of the type $\gamma(t) = \gamma_0 \sin(\omega t)$. Here, $\gamma(t)$ is the instantaneous strain, γ_0 is the strain amplitude of the sinusoidal signal, and ω is the angular frequency. Within the linear viscoelastic regime (LVER), the stress response to an applied sinusoidal strain can be described by a single odd harmonic ($I_1 \equiv \sigma_1$) from which the conventional storage (G') and loss (G'') moduli can be retrieved.[55,56] Above the LVER regime, the onset of nonlinearities causes a distortion of the simple sinusoidal response, and the stress can be decomposed as:

$$\sigma(t) = \sum_{n=1\,odd}^{N} \sigma_n \sin(n\omega t + \delta_n) \qquad (2)$$

In eqn (2), n is the number of harmonics of a Fourier series, σ_n is the stress associated to the harmonic number n, equivalent to the intensity of the nth harmonic (*i.e.*, I_n), and δ_n is the phase angle. Due to the odd symmetry in the shear stress response relative to the shear direction,[56,57] only the odd harmonics are used to decompose the stress signal. Among the higher harmonics, the third harmonic ($I_3 \equiv \sigma_3$) consistently exhibits the greatest magnitude. Therefore, the ratio I_3/I_1 is frequently employed to quantify the level of nonlinearities within the sample.[55,57] Still, the higher odd harmonics can be used to reconstruct the total stress signal, which can be further analysed through the SPP method to obtain insights into the intracycle transformations experienced by the material.

The SPP framework offers a unique method for interpreting stress signals for any type of material. For complex materials that exhibit neither purely elastic nor purely viscous behaviour, the stress response $\sigma(t)$ to a periodic deformation depends on both the applied strain $\gamma(t)$ and the induced shear rate $\dot{\gamma}(t)$. This translates into a three-dimensional visualisation of the stress response within a single deformation period, where the axes of this space are given by the instantaneous deformation, the normalised instantaneous shear rate and the stress, $[\gamma(t), \dot{\gamma}(t)/\omega, \sigma(t)]$. Projections of this 3D curve onto the $[\gamma(t), \sigma(t)]$ and $[\dot{\gamma}(t)/\omega, \sigma(t)]$ planes provide the classic Lissajous–Bowditch curves.[52,57] The specific physical processes governing the material's response during each sinusoidal deformation cycle influence the dynamic evolution of the 3D stress trajectory. Using infinitesimal steps, the instantaneous tridimensional stress can be decomposed into two components: one in phase with the strain (representing the instantaneous elastic contribution, G'_t) and one in phase with the shear rate (representing the instantaneous viscous contribution, G''_t). These instantaneous moduli
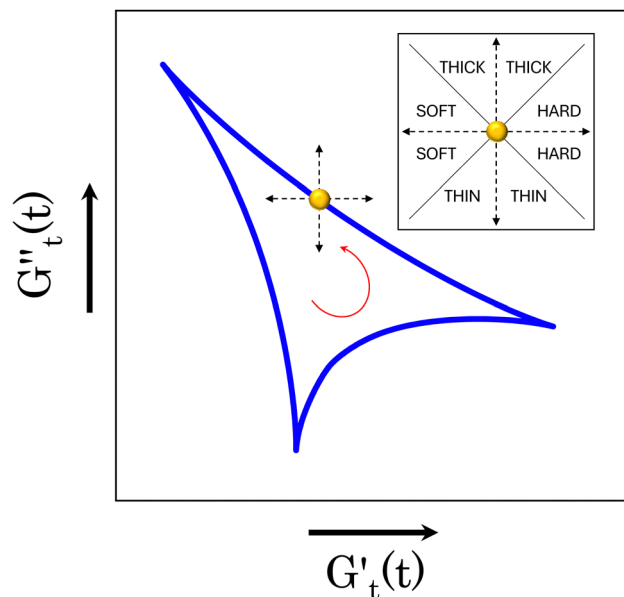

Fig. 1 Example of a Cole–Cole plot. A schematic of the type of transition experienced by the material, depending on the direction of the trajectory, is reported at the top corner of the panel. For instance, taking the yellow point and following the blue trajectory anti-clock wise, the instantaneous storage modulus is decreasing, while the instantaneous loss modulus is increasing. This indicates a simultaneous softening and thickening of the material.

are defined as partial derivatives of the stress with respect to the strain and the shear rate, allowing for a clear separation of elastic and viscous contributions. For the complete mathematical derivation please refer to Rogers' original work.[51] All rheological transitions within a deformation cycle can be described by the changes in these two instantaneous moduli. For easier visualisation, these changes are typically reported in a Cole–Cole plot (Fig. 1). This graphical representation allows for straightforward interpretation of the evolving rheological behaviour during each strain cycle. Horizontal movements on the plot indicate elastic changes, with an increase in G'_t signifying stiffening and *vice versa*. Similarly, vertical movements represent viscous transitions, with an increase in G''_t indicating thickening and *vice versa*.[51–54] For infinitesimal strain amplitudes, the trajectories would converge to a single point representing the bulk storage G' and loss G'' moduli, signifying the absence of any microstructural rearrangements within the material, as expected in the LVER.

2.4 Drug release tests

The transdermal delivery performance of the Pes was evaluated using permeation studies of levosimendan in a Franz cell. The Franz cell, equipped with a hydrophobic polysulfone membrane (0.45 μm porosity, Omicron Research Ltd), mimics the permeation process through the skin (a schematic of the cell can be found in the ESI,† Fig. S.1A). A stock solution of levosimendan (0.1 mg mL^{-1}) was prepared in jojoba oil and then emulsified with aqueous microgel solutions as described in Section 2.3. For each formulation, 1 mL of the emulsion was placed in the

donor chamber, resulting in a consistent total drug mass of 0.05 mg (as half the volume of each formulation is oil). Standard PBS buffer solution (5 mL) served as the receiver phase. Samples (2 mL) were periodically withdrawn from the receiver compartment and replaced with fresh buffer solution to maintain a constant volume throughout the 190-hour experiment. The concentration of released levosimendan at each time point was measured using a double-beam Cary-60 UV-vis spectrometer (Agilent UK) at 400 nm. The instrument was initially calibrated using a series of 10 levosimendan solutions at known concentration in PBS buffer (Fig. S.1B in ESI†). The cumulative percentage of drug released (CR%) was then calculated as $CR\% = c_R/c_0 \times 100$, where c_R is the concentration of levosimendan accumulated in the receptor chamber at a specific time, and c_0 is the initial drug concentration. To assess the permeability of the drug to the polysulfone membrane, a reference experiment was conducted using a simple jojoba oil solution containing levosimendan (0.05 mg mL^{-1}) (Fig. S.1C in ESI†). All experiments were performed at both room temperature ($T = 21$ °C) and physiological temperature ($T = 37$ °C) to investigate the thermoresponsive behaviour of the Pes on sustained release.

3 Results and discussion

3.1 Microgels sizes and surface charge

The DLS results, reporting the average sizes of the pNIPAM-co-BVI microgels used to stabilise the Pickering emulsions are reported in Fig. 2A as a function of temperature. An average swollen diameter of 348 ± 4 nm and 796 ± 44 nm is found for samples M300 and M800, respectively at 20 °C. The microgels show the same qualitative behaviour of conventional pNIPAM microgels. At low temperatures, the crosslinked cores swell to their maximum dimension thanks to the higher hydrophilicity of the NIPAM chains. As the temperature increases, the polymer becomes more hydrophobic, causing a collapse of the network and a reduction of the microgels diameters. The temperature transition is consistent for both microgels, showing a lower critical solution temperature (LCST) around 32.5 °C, which corresponds to the typical value reported for pNIPAM in the literature.[25,46,58] However, a difference is observed in the shape of the volume transition, when the average diameters are normalised with the values obtained at $T = 20$ °C ($d_{p(20°C)}$). In both cases, the microgels shrink linearly with temperature, until reaching the LCST, where the diameters suddenly collapse to half the original size (inset in Fig. 2A). Bigger microgels present a more pronounced gradient, showing a final collapse of more than half the original swollen size. In addition, a higher variability is observed for the measured sizes of microgels M800 in the swollen configuration, as highlighted by the larger error bars in Fig. 2A. Both aspects can be related to the core–shell morphology of pNIPAM-MGs, characterised by a denser crosslinked core and external dangling ends.[58,59] These external chains are typically longer for bigger microgels and therefore can assume a wider range of relaxed conformations,
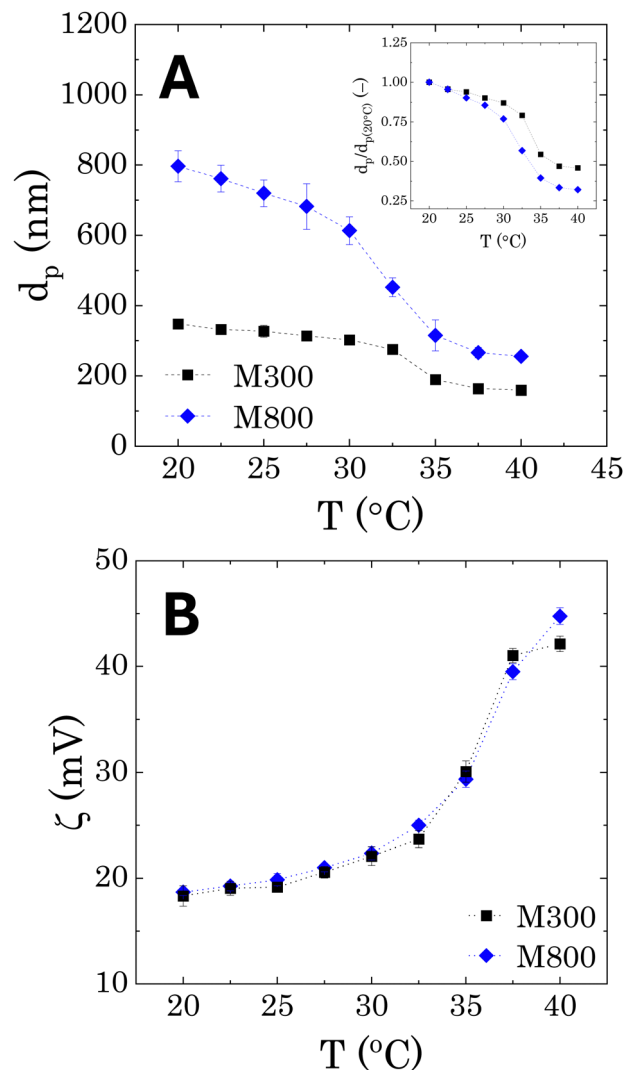

Fig. 2 Temperature dependent measurement for pNIPAM-co-BVI microgels of different sizes. (A) Hydrodynamic diameter obtained from DLS measurements; (B) zeta-potential. The error bars represent the standard error between an average of 5 different measurements. The inset in panel (A) shows the hydrodynamic diameters normalised by $d_{p(20°C)}$.

which will affect the hydrodynamic diameter of the microgel particles and their temperature-dependent transition.[58–60]

In terms of surface charge (Fig. 2B), the zeta-potential measurements show a positive charge of approximately +18 mV, which is related to the presence of BVI at the external periphery of the microgels.[25] We note that, as already found in the literature for pNIPAM microgels, as the particle shrinks at increasing temperatures, the surface charge increases because of a higher charge density in the external boundary of the microgels.[61] Overall, the two microgels do not show any differences in surface charge, indicating a similar binding efficiency of the external BVI molecules.

3.2 Calculation of microgels effective volume fraction

To estimate the degree of coverage of the MG-stabilised drops and obtain a proper comparison between different MG sizes,

the effective particle volume fraction (ϕ) and in turn the number concentration (n_p) need to be calculated. The effective ϕ can be found using a rheological approach. For suspensions of repulsive particles, it is in fact predicted that the relative zero-shear viscosity is a function of the particle volume fraction, usually showing divergence as the critical jamming concentration is approached.[62,63] If a linear relation is assumed between the mass concentration c and the resulting volume fraction ϕ, expressed as $\phi = k_M c$, the constant k_M can be determined by fitting the measured relative zero-shear viscosity of the MG suspensions, $\eta_r(c)$. In Fig. 3, we report the results for microgels M300 and M800. Both sets of data can be fitted together with the equation derived by Mooney[64] for concentrated suspensions of spherical particles:

$$\eta_r = \exp\left(\frac{2.5 k_M c}{1 - \lambda k_M c}\right) \quad (3)$$

where, λ is a fitting parameter related to the maximum packing factor that the system can achieve and it can vary as follows, $1.2 < \lambda < 1.9$. The equation derived by Mooney has been developed for hard spheres by adding a crowding parameter to the Einstein equation for infinitely diluted systems. Although developed for hard spheres, it has been successfully applied to soft systems such as emulsions[64] and microgels.[63] The fitting yields $k_M = 8.42$ and $\lambda = 1.244$. If we consider that ϕ and n_p are related as follows:

$$\phi = n_p \frac{4}{3}\pi\left(\frac{d_p}{2}\right)^3 \quad (4)$$

we can then retrieve the number concentration of microgels, used to calculate the theoretical surface coverage (C).

Note that in previous works, n_p was obtained assuming an effective density of the microgels, which takes into account their porosity.[24,65,66] This method does not consider possible changes in the swollen conformation of the microgels and can overestimate the effective volume fraction of the microgels.
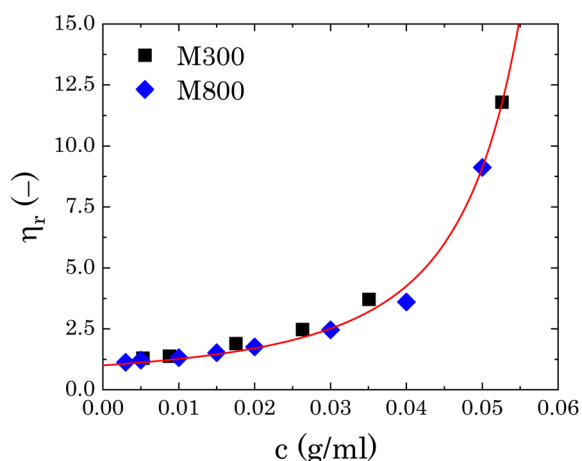

Fig. 3 Relative viscosity as a function of microgel mass fraction for both sets of microgels. The red line is the fitting of eqn (3) to the experimental points.

3.3 Pickering emulsions – appearance and droplet size distribution

The general appearance and droplet size distribution (DSD) of Pickering emulsions stabilised with microgels M300 and M800 were investigated at various microgel loadings. The appearance of the PEs is significantly influenced by the size of the microgel particles. Regardless of the microgel concentration, samples stabilised with smaller particles appear smooth and fluid, whereas those stabilised with larger microgels have a paste-like consistency with a granular texture (Fig. S.2 in ESI†). As the microgel content decreases, samples stabilised with M300 microgels become more prone to creaming, evidenced by the residual layer of aqueous microgel dispersions at the bottom of the test vials. In contrast, PEs stabilised with larger M800 microgels do not show any creaming, with only a small amount of water visible at the bottom of the test vial at the lowest microgel concentration (sample M800-C3 in Fig. S.2). As opposed to M300-stabilised samples, in this case, the water layer appears transparent, indicating that most microgels remain in the emulsion phase. This suggests differences in the stabilising mechanism of the two microgel sizes. To further investigate these differences at the microscale, we analysed the characteristic DSD of all the samples using bright-field, fluorescent, and confocal microscopy. An example of the images obtained from bright-field microscopy, along with the corresponding droplet size distributions, is shown in Fig. 4.

Both microgel size and concentration have a direct effect on the size distributions of the droplets obtained. For smaller microgels, i.e. sample M300, small droplets with average sizes around ~ 5 μm and a fairly narrow size distribution are observed for both samples C1 and C2. However, at the lowest concentration, there is a significant shift towards larger droplet sizes, reaching an average size of approximately ~ 25 μm, with a broad size distribution. A more progressive shift of the size distributions is instead observed for PEs stabilised with microgels M800. Similarly to sample M300, the highest microgel concentration, sample M800-C1, shows an average size of ~ 5 μm, but the average droplet diameter increases with a decrease in microgels loading, yet maintaining fairly narrow size distributions. A plot summarising the average droplet sizes (eqn (1)) for all samples is reported in Fig. 5A. In the graph, the average sizes are reported against the number of microgels available in the aqueous phase, normalised by the theoretical number required to obtain a coverage of 0.78 (i.e., limit of maximum random packing of spherical objects in 2D[67]), for a fixed average droplet size equivalent to the process-controlled dimension (i.e., ~ 5 μm). Typically, above the limited coalescence threshold, i.e. when particles are in excess, the average droplet size of Pickering emulsions is primarily determined by the details of the emulsification process.[27,68] For a given set of fluids, the key factors influencing droplet size are the geometry of the homogeniser, the rotational speed, and the homogenisation time. Once these parameters are fixed, the initial drop size created by the homogeniser remains constant because there are enough particles to cover the interface of the drops. With a decrease in particle concentration, a diminishing proportion of
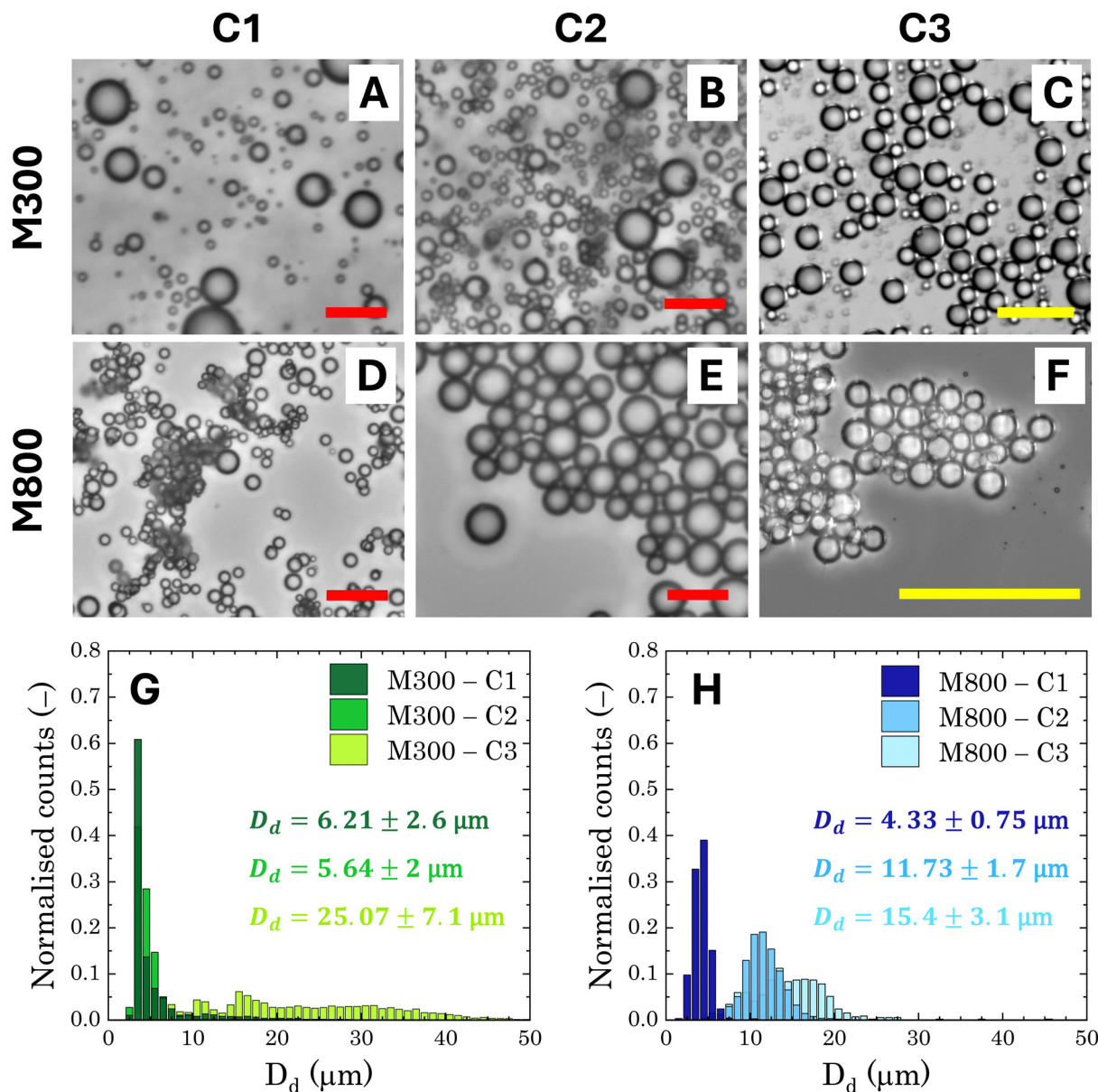
Fig. 4 Droplet size distribution of the microgels stabilised Pickering emulsions. Micrographs of PEs stabilised with microgels M300/M800 at different microgels mass fractions, (A) and (D) C1 – 6 wt%, (B) and (E) C2 – 4 wt%, (C) and (F) C3 – 2 wt%. The red scale bar corresponds to 20 μm, while the yellow scale bar corresponds 100 μm. Normalised droplet size distribution of PEs stabilised with (G) M300 and (H) M800 microgels. The distributions are obtained by measuring the size of >2000 droplets for each sample.

the interface remains shielded by particles. This facilitates droplet coalescence until a stable size is achieved.[27]

In the present system, the average attainable droplet size is around 5 μm, as demonstrated by the average sizes observed at the highest microgel loadings. However, while the onset of the limited coalescence regime occurs at a normalised particle number of 1 for small microgels, as expected, the threshold is shifted to lower values for larger microgels. This shift indicates that fewer large microgels are needed to stabilise the average size of the droplets at the process-controlled size, highlighting a fundamental difference in the microstructure of emulsions stabilised with different microgel sizes. Thanks to their more homogeneous crosslinking distribution, smaller microgels are expected to form a more uniform and densely packed shield around the droplets, resulting in emulsions with droplets that are less prone to aggregation.[27] Conversely, large microgels result in Pickering emulsions with a more heterogeneous coverage, which are more prone to droplet adhesion. In particular, the increased adhesion has been attributed to a bridging effect, due to the presence of shared microgels simultaneously adsorbed at the interface of two droplets.[27] This phenomenon is favoured in the presence of larger microgels because, once adsorbed at the interface, they present a lower mobility, resulting in a more disordered coverage.[69] This leaves free interface
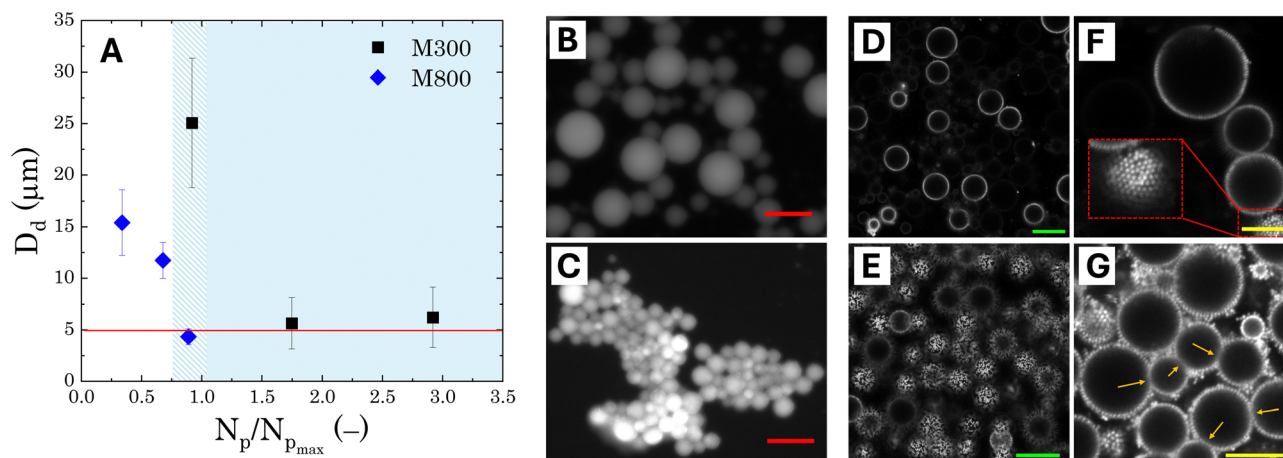
Fig. 5 (A) Average droplet size *versus* number of microgels available in the aqueous phase, normalised by the theoretical number required to obtain full droplet coverage. The red line is a guide for the eye to show the homogenisation-limited droplet size, while the coloured panel highlights the region where the size is controlled by the homogenisation procedure. The error bars represent the standard deviation of the size distribution. Fluorescence images showing details of droplets aggregations for PEs stabilised with microgels (B) M300-C3 and (C) M800-C2. The red scale bar represents 25 μm. Confocal microscopy images of diluted samples (D)–(F) M300-C1 and (E)–(G) M800-C1 showing the assembly of the microgels at the droplets interface. In panel (F), the inset reports a detail of the droplet interface, showing a packed microgel organisation. The green scale bar represents 20 μm, while the yellow scale is equivalent to 10 μm. The arrows in panel (G) highlight the points of bridging between droplets.

for other microgels, allowing bridging between two droplets. Fluorescence micrographs confirm this scenario: stable 3D clusters of droplets are clearly identifiable in samples prepared with M800 microgels (Fig. 5C), while more dispersed and solitary droplets are observed in samples prepared with M300 microgels (Fig. 5B). Confocal microscopy reveals additional details regarding the assembly of microgels. Samples stabilised with M300 exhibit a uniform microgel coating, as evidenced by the consistent ring surrounding the droplets (Fig. 5D–F) and the packed assembly of the microgels at the droplet interface (inset in Fig. 5F). In contrast, M800-stabilised samples display a less dense microgel distribution. Here, we observe droplets with exposed areas (Fig. 5E) alongside bridged droplets where microgels appear shared at the interface (Fig. 5G). Given the charged nature of the microgels, beyond the direct effect of different microgel morphologies, electrostatic interactions can also contribute to the discrepancy observed. While the presence of charges contributes to a more ordered interfacial structure for small sizes, this has no effect on large microgels, where the interactions, and thus the interfacial organisation, are prevalently dominated by volume effects.[28]

Overall, the microscopic analysis confirms what already reported in the literature,[27,69] showing significant differences in the microstructure of the Pickering emulsions obtained with the two different microgel sizes. These differences in microgels arrangement and interfacial coverage can have a profound impact on the rheological behaviour of the formulations. For instance, a more dispersed droplet distribution with minimal inter-droplet connections would likely exhibit more fluid-like behavior. This translates to lower viscosities, which in turn, would lead to faster release kinetics due to the increased diffusion coefficients. Conversely, the presence of droplet clusters, could introduce more pronounced elastic properties,

which can influence the mobility of the emulsion, thus inducing slower release properties. Therefore, investigating the nonlinear rheological properties is fundamental to provide further insights into the connection between microstructure and performance.

3.4 Rheological characterisation

3.4.1 Nonlinear viscoelastic properties – intercycle transitions. Strain amplitude oscillatory sweep measurements were performed to probe the changes in the mechanical properties of the PEs induced by stabilisation with different microgel sizes. This characterisation is particularly valuable for revealing the microstructure of emulsions and colloidal suspensions[35,54,55,63,70,71] through their yielding behaviour.

Fig. 6A illustrates the dependence of the storage (G') and loss (G'') moduli on the strain amplitude for all the investigated samples, measured at an oscillation frequency $\omega = 10$ rad s^{-1}. All the PEs exhibit a type III strain response,[72] characterised by an elasticity-dominated linear viscoelastic regime (LVER) at low strains, and a G'' overshoot. At low strain amplitudes, G' maintains a constant plateau, exceeding G''. As the strain increases, a crossover is observed where G'' surpasses G', while going through an overshoot. The crossover point indicates the final threshold of the strain-induced solid-to-liquid transition, and it is followed by a decrease of both moduli at higher strain amplitudes (strain-thinning). This type of response is commonly observed in soft glassy and jammed materials,[53,63,73] and reflects the microstructural rearrangements that the material undergoes during the yielding process. At low strains, the viscoelastic response is dominated by the elastic restoring force of the jammed dispersed phase,[74–76] in this case represented by the Pickering droplets. As the strain amplitude increases, the stress applied overcomes the elastic response, and the droplets
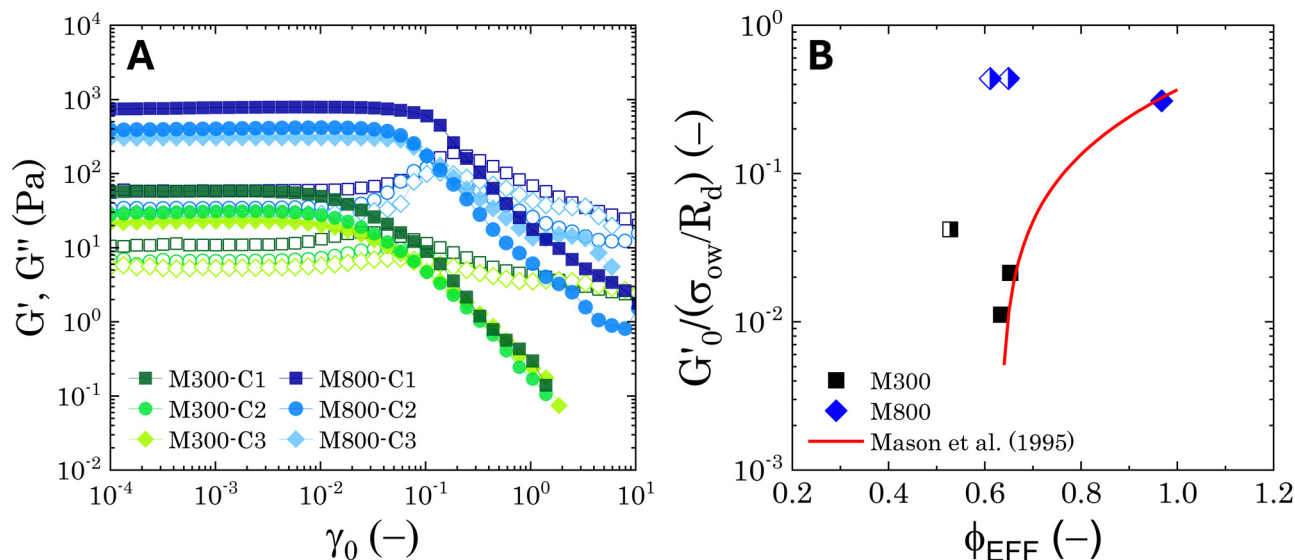
Fig. 6 Average viscoelastic moduli from strain amplitude oscillatory tests. (A) Strain amplitude dependence of the storage (closed symbols) and loss (hollow symbols) moduli obtained from strain amplitude oscillatory experiments at $\omega = 10$ rad s^{-1} for the Pickering emulsions tested. (B) Zero-shear plateau storage modulus $\left(G_0'\right)$ scaled by the Laplace pressure of the dispersed droplets ($\sigma_{\text{ow}}/R_{\text{d}}$), plotted against the effective dispersed volume fraction (ϕ_{EFF}) defined as in Kaganyuk and Mohraz (2019).[33] Red line is the prediction found by Mason *et al.* (1995),[30] $G_0'/(\sigma/R_{\text{d}}) \sim \phi(\phi - \phi_{\text{c}})$, where $\phi_{\text{c}} \approx 0.635$. Half-filled symbols highlight the points that do not align with Mason's prediction.

escape their positions at rest, sliding against each other, thus enabling the material to flow (crossover point). The transition between the elasticity-dominated and the liquid-like responses, *i.e.* the yielding transition, is progressive and encompasses various microstructural rearrangements, which culminate in the peak of the viscous component, associated to the release of energy dissipated during the reorganisation of the material.[53,63,76]

Despite the similarities in the general trends, PEs stabilised with different microgel sizes exhibit some key distinctions. PEs stabilised with small microgels display lower elasticity, as shown by the lower LVE plateaus of G' in Fig. 6A, and a shorter extension of the LVER. The impact of microgel loading on the overall viscoelastic behaviour appears small for PEs stabilised with the same microgel size. While a slight reduction of the elastic plateau $\left(G_0'\right)$ is observed for both types of PEs as microgel concentration decreases (Fig. S.3 in the ESI†), there is a significant jump between M300 and M800-stabilised PEs, even though the oil fraction remains constant across all formulations. To accurately account for these observed differences, G_0' should be reported as a function of the effective dispersed phase volume fraction (ϕ_{EFF}). This metric considers the increased volume fraction due to the microgel monolayer at the droplet interface.[33] Additionally, changes in microgel loading also affect droplet size in both PE sets, which is known to influence the elastic modulus plateau.[30,33] Therefore, to account for both factors, we normalise G_0' by the Laplace pressure of a single droplet, $\sigma_{\text{ow}}/R_{\text{d}}$, and report it as a function of ϕ_{EFF} (for details on the calculation of ϕ_{EFF}, please refer to Section S5 of the ESI†). Here, σ_{ow} is the interfacial tension between the oil phase and the aqueous microgel dispersion

(see Table S.3 in the ESI†), and $R_{\text{d}} = D_{\text{d}}/2$ is the average droplet radius.

Fig. 6B presents these results alongside the predictions of Mason *et al.*[30] The scaling suggests that the elastic moduli of the samples tested follow the prediction only at high effective volume fractions higher than $\phi_{\text{c}} \approx 0.635$. Although measures at multiple volume fractions are required to confirm the generality of the trend for the system at hand, this hints towards a shift in the dominant factors governing elasticity. At high ϕ_{EFF}, when the dispersed phase is effectively jammed, the elasticity of the material is primarily determined by the elasticity of the individual droplets. In contrast, at lower ϕ_{EFF}, the long-range structuring of the PEs becomes more important for elasticity. For M300-stabilised PEs, the higher elasticity observed at lower ϕ_{EFF} (*i.e.*, sample M300-C3) can be attributed to the presence of excess microgels in the continuous phase (see Tables S.1 and S.2 in the ESI†), which can likely influence droplet interactions near the jamming threshold. In fact, for sample M300-C3, $\phi_{\text{EFF}} \approx 0.53$ and the total volume fraction of the dispersed phases (*i.e.*, $\phi_{\text{TOT}} = \phi_{\text{EFF}} + \phi_{\text{m}}$, where ϕ_{m} is the volume fraction of excess microgels) reaches a value of $\phi_{\text{TOT}} \approx 0.59$. Conversely, for M800-stabilised PEs, the sustained elasticity at lower ϕ_{EFF} is likely due to the presence of droplet clusters, which contribute to a more robust structure even at lower effective volume fractions. Notably, deviations from the LVE behaviour occur at strains $\gamma_0 \sim 10^{-2}$ and $\gamma_0 \sim 10^{-1}$ for PEs stabilised with microgels M300 and M800, respectively. The shorter LVER for M300-stabilised PEs indicates a lower tolerance for deformation, and therefore stress, before yielding.[71,77] This translates in a significant difference in the yield stress (σ_y) observed for the PEs stabilised by the two different microgel sizes (see Fig. S.3B, ESI†), which differ of two orders of magnitude. These results

suggest smaller microstructural units within the material, and they align with the microscopy data, which show no tendency for clustering in PEs stabilised by small microgels. In this case, the "cage" formed by surrounding droplets can be considered as the microstructural unit. Conversely, the presence of droplet clusters in PEs stabilised by M800 microgels implies a more intricate yielding process. Here, droplets rearrange within the cluster before complete yielding occurs. This is further supported by the higher normalised peaks of the loss moduli observed for M800-stabilised samples compared to M300 (see Fig. S4 and S7, ESI†), which highlight the higher dissipation associated to multiple rearrangements.[78,79]

Following the G'' overshoot and the crossover point where G'' surpasses G', both types of PEs exhibit a similar strain-thinning behaviour, with both G' and G'' following a power-law decay of the type $G' \sim \gamma^{-\mu}$ and $G'' \sim \gamma^{-\nu}$, with a ratio $\mu/\nu \sim$ [2.2–3.1]. This aligns with observations for soft glassy materials.[63,79,80] Interestingly, for both PE systems, a second shoulder appears in the strain dependence of the loss modulus as the microgel loading is reduced. This is more evident in the normalised moduli presented in Fig. S.4A and B (ESI†), where a smaller peak can be observed around $\gamma_0 = 1$–10. The presence of this secondary peak in G'' is often associated with a more complex microstructure. In such cases, the flow transition involves a sequence of microstructural rearrangements at different scales: smaller-scale rearrangements within clusters (e.g., droplet rearrangement) and larger-scale rearrangements involving cluster breakage.[71,78,79]

These observations suggest the occurrence of complex yielding phenomena within the PEs. The presence of a multi-step flow transition and the dependence on microgel loading point towards a strong interplay between the microstructure and the mechanical response of the Pickering emulsions, motivating further investigation into the intracycle nonlinear stress response using quantitative methods.

3.4.2 Nonlinear viscoelastic properties – intracycle transitions. The average G' and G'' obtained from strain amplitude oscillatory rheological tests represent the true elastic and viscous contributions of a material only within the LVER. Beyond the LVE threshold, the elastic and viscous components become nonlinearly entangled.[49,57] Hence, to gain further insight into the microstructure of the PEs under these conditions, we investigate the time-dependent stress response during a full cycle of the sinusoidal deformation using Fourier-Transform (FT) decomposition of the signal and the sequence of physical processes (SPP) analysis. Fig. 7 presents the results for two key parameters that quantify the nonlinear behaviour of the PEs during oscillatory shear. The first is the ratio of the third to the first harmonic (I_3/I_1), which provides an estimate of the degree of nonlinearity in the material's response. Higher values of I_3/I_1 indicate a more pronounced deviation from linear viscoelastic behaviour.[52,55,57,70] The second parameter is the dissipation ratio (DR), which serves as an indicator of the energy dissipation mechanisms during yielding. This quantity can be obtained as a ratio between the total energy dissipated per unit volume in a single cycle of

deformations, calculated as $E_d \equiv \oint \sigma \mathrm{d}\gamma = \pi\gamma_0^2 G''$, and the energy dissipated by a perfect plastic material at the same deformation value, obtained as $E_{dp} = 4\gamma_0\sigma_{max}$, where σ_{max} is the maximum stress reached by the material during a full cycle.[55,81] Following this definition, the dissipation mechanism can be classified in three extreme behaviours: (i) DR $\equiv E_d/E_{dp} = 1$ purely plastic deformation, (ii) DR = 0 purely elastic deformation, (iii) DR = 0.785 Newtonian fluid deformation.[81]

While no significant dependence on microgel loading is observed for either microgel sizes (M300 or M800), the results reveal clear differences in the nonlinear behaviour between the two PEs types. For M300-stabilised PEs, above the instrumentation limits (i.e. semi-transparent symbols in Fig. 7A and B), the coefficient I_3/I_1 follows a power-law trend with an exponent of approximately 2 within the MAOS region, where yielding occurs. This aligns with observations in the literature, which report a similar coefficient for soft glassy systems.[55,82] Beyond the MAOS region, I_3/I_1 plateaus at a constant value of approximately 0.25. In contrast, M800-stabilised PEs exhibit a sharper rise in the I_3/I_1 ratio, starting just before the end of the LVER, and increasing with a power-law exponent slightly higher than 2 during yielding. This sharper rise, corresponding to a narrower yielding window, is then followed by a first plateau at 0.36, a second small rise around $\gamma_0 = 3$, and finally another plateau at a higher value of 0.65. The higher plateau values, together with the occurrence of multiple flow steps, suggest stronger nonlinearities associated to multiple restructuring events within the emulsions. Here, smaller-scale rearrangements within clusters might occur first, followed by cluster breakage at higher deformations. Notably, the presence of these plateaus indicates that the emulsions maintain some structure even at high deformations and for effective volume fractions below 0.64 (as observed for sample M800-C3).

Similar conclusions can be drawn from the analysis of the dissipation ratio, Fig. 7C and D. In the initial LVER, for both PE types, the low DR values indicate a predominantly elastic response. Specifically, for M800-stabilised PEs, the initial DR plateaus at around 0.065 for all microgel loadings. Conversely, M300-stabilised PEs exhibit some variability, with progressively higher LVE plateaus ranging from 0.14 to 0.2, indicating overall a bigger deviation from the pure elastic regime compared to M800 samples. A sharp increase in DR is observed as the LVER is surpassed. Notably, for samples M800, DR increases with a power-law of 2 during yielding, independent of microgel loading. In contrast, M300-stabilised PEs display a smoother increase with a power-law of approximately 0.5 (see Fig. S.5 in the ESI,† for log-scale plots). After the yielding transition, the DR for M800 samples plateaus at high values ∼0.9, indicating a tendency towards plastic dissipation.[55] Conversely, M300-stabilised PEs exhibit a peak in plasticity, just after yielding, followed by a return to a Newtonian-like behaviour. This further corroborates the structural differences between the two PE types, with M800-stabilised PEs exhibiting greater interconnectivity and more microstructural rearrangements. To gain further insights into the transient rheological behaviour that these two types of PEs undergo during larger strain amplitudes,
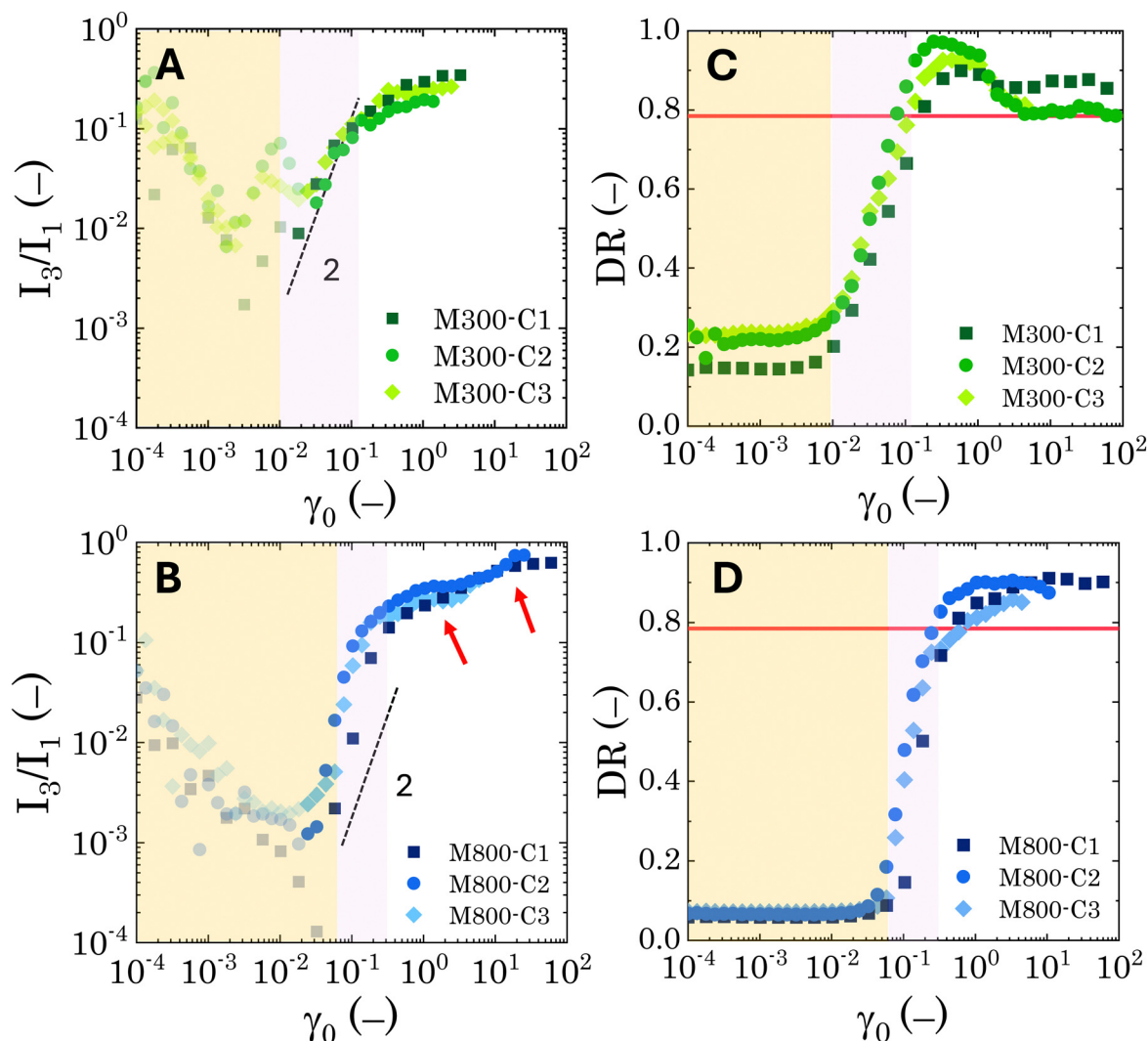
Fig. 7 Nonlinear parameters obtained from strain amplitude oscillatory tests. Trend of the I_3/I_1 ratio *versus* the nominal strain amplitude for different microgel loadings for (A) M300- and (B) M800-stabilised Pickering emulsions. Semi-transparent symbols indicate points dominated by instrumentation noise. In both panels, the dash black line is a guide for the eye for a power-law of 2. The red arrows in panel (B) highlight the two plateau regions observed for M800-PEs. Dissipation ratio *versus* the nominal strain amplitude for different microgel loadings for (C) M300- and (D) M800-stabilised Pickering emulsions. The continuous red line in both panels indicates the Newtonian threshold of 0.785. In all panels the yellow background shows the extension of the LVER, while the pink one shows the yielding transition region up to the G' and G'' crossover point.

we report the evolution of the Cole–Cole trajectories of the transient storage (G'_t) and loss (G''_t) moduli for two indicative samples, *i.e.* M300-C1 and M800-C1 (Fig. 8A and B).

The Cole–Cole plots for both samples exhibit the characteristic deltoid shape, reflecting the dominance of the third harmonic.[52,54,83] However, the orientation and enclosed area of the cycles progressively change with increasing strain amplitude. These two features offer valuable insights into the sequence of microstructural rearrangements the material undergoes during each oscillation cycle. The orientation of the trajectory reflects the nature of the material's deformation transition, while the enclosed areas relate to the extent of intracycle rheological transitions. A larger enclosed area indicates a broader spectrum of microstructural rearrangements within the material.[55,83] Notably, in the LVER the size of the deltoids

in both cases is significantly small, with the values of G'_t and G''_t converging to the values of G'_0 and G''_0, respectively. Increasing strain amplitude leads to a departure from linearity, as evidenced by the evolving orientation and size of the deltoid curves in the Cole–Cole plots (Fig. 8A and B). Interestingly, key distinctions in the evolution are observed between the two PEs types. For M300-stabilised PEs, the deltoid trajectories maintain a similar orientation after departing from the LVER (*e.g.*, magenta curve in Fig. 8A) and the areas progressively grow until the final yielding point (see Fig. S.6 in the ESI,† reporting the evolution of the areas of the deltoids, A_D, normalised by the area in the LVER, A_{D0}). Beyond this point, the size of the deltoids decreases again, until reaching very small areas at $\gamma_0 > 1$. These results imply that PEs stabilised with small microgels undergo their widest range of microstructural rearrangements
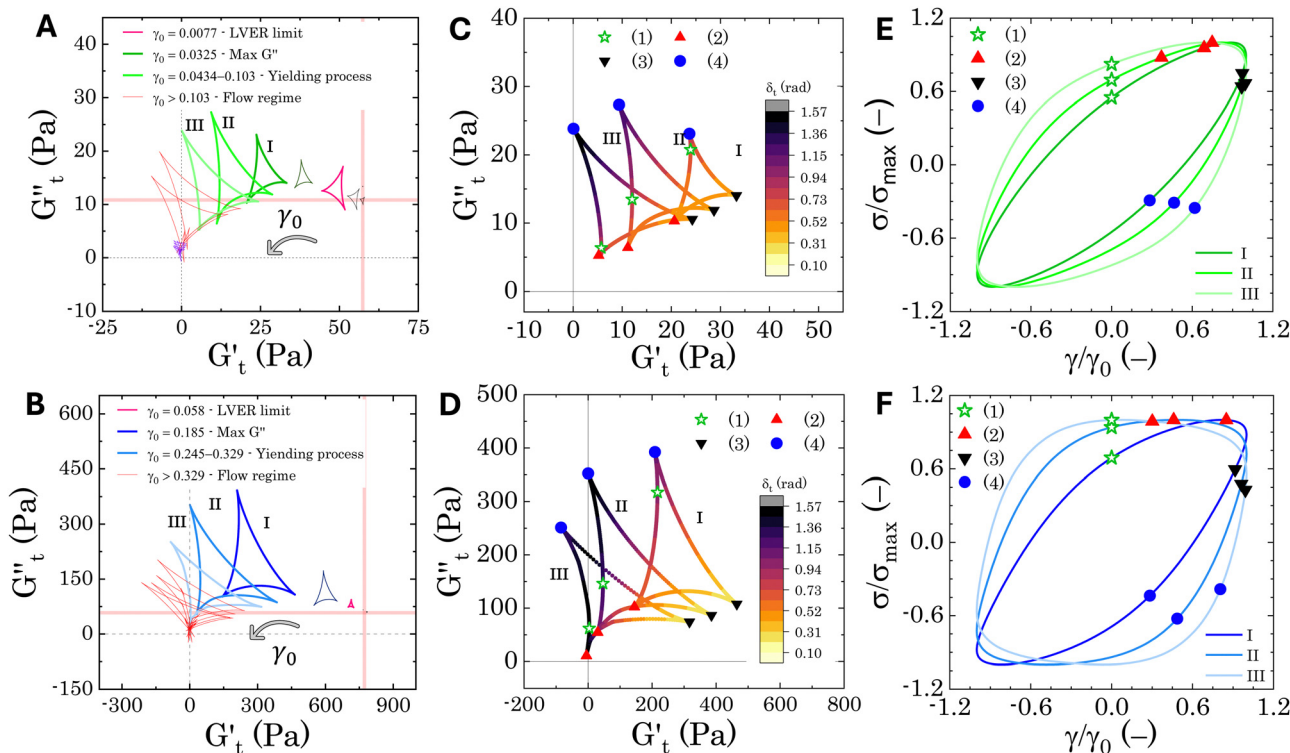
Fig. 8 Sequence of physical processes (SPP) analysis: Cole–Cole plots and material response. Panels (A) and (B) show representative Cole–Cole plots for samples M300-C1 and M800-C1, respectively. Panels (C) and (D) detail the intracycle transformations observed in the yielding region (trajectories I, II, and III) for samples M300-C1 and M800-C1, respectively. The colormap represents the instantaneous phase angle δ_t experienced during each deformation cycle. Symbols depict the sequence of transitions the material undergoes within each half-cycle (1 to 4). Finally, panels (E) and (F) display the Lissajous–Bowditch plots corresponding to the trajectories shown in (C) and (D) for samples M300-C1 and M800-C1, respectively.

around the yield point, where the solid-to-liquid transition is accompanied by some degree of structural recovery.[54,55,83] However, at even higher strains, the structure breaks down more severely, hindering recovery and leading to a complete collapse of the microstructure. In contrast, the area changes for M800-stabilised PEs exhibit a less gradual increase, with a rapid rise observed around the G'' overshoot. After the yield point, the areas decrease progressively but remain at relatively high values (see Fig. S.6 in the ESI†). This trend reinforces the presence of a more interconnected network within PEs stabilised by larger microgels. Here, the droplet clusters are capable of yielding and recovering within each deformation cycle, demonstrating resilience against complete breakdown at the tested amplitudes. The difference in microstructure between the two types of PEs is further evident in the details of the trajectories around the yielding point.

In Fig. 8C and D, we report the trajectories obtained for M300- and M800-stabilised PEs, respectively, including a colormap of the instantaneous phase angle, δ_t. This value directly indicates the type of transition the material undergoes at each point within the deformation cycle. Typically, $\delta_t < 0.785$ suggest elastic behaviour, while values exceeding 0.785 indicate liquid-like behaviour.[53,55] The colormap clearly reveals that sample M800-C1 experiences more extensive structural rearrangements. This is evident from the wider range of δ_t values spanned within a single cycle for this sample compared to

M300-C1. In particular, M300-C1 exhibits a more progressive yielding process (Fig. 8C–E). Trajectory **I**, starting from an initial instantaneous strain equal to zero (point 1), shows a strong initial thinning with minimal softening, leading to a minimum in both G'_t and G''_t at point 2. During this transition, both the strain amplitude and the total instantaneous stress are increasing, as can be seen in the Lissajous-Bodwditch plots in Fig. 8E, indicating the breakdown of the initial structure as strain increases. As the strain reaches its maximum and reverses (point 2 to 3), the emulsion experiences a restructuring, indicated by rising G'_t and G''_t values (coupled thickening/stiffening). As the flow reverses in the opposite direction, approaching again an instantaneous strain of zero, the structure breaks down, dissipating stored elasticity and reaching a maximum G''_t (point 3 to point 4). Beyond this point, the structure thins again, returning to its initial state and repeating the cycle. This qualitative behaviour persists at higher nominal strain amplitudes (trajectories **II** and **III**), with a gradual reorientation of the deltoids towards a more plastic response. The initial stress increase becomes weaker, and the structure exhibits more liquid-like behaviour later in the cycle, as shown by the δ_t colormap.

Sample M800-C1 displays a different response around the yielding point (Fig. 8D–F). Trajectory **I**, corresponding to the G'' overshoot, shares some similarities with M300-C1, but the δ_t

colormap indicates a wider range of restructuring within the material. As the strain amplitude increases (trajectory **II**), the behaviour transitions to a plastic-type response, as shown by the quasi-constant stress response with an increase of the instantaneous strain amplitude (point 1 to 2 in Fig. 8F), followed by strain-thinning at a higher nominal strain amplitude (trajectory **III**). This transition corresponds to the G'/G'' crossover point. Here, G'_t becomes negative and the total stress slightly reduces, indicating a softening of the microstructure and suggesting complete material flow (1 to 2). As the strain increases further and reverses, the structure first undergoes a nearly purely viscous thickening, followed by purely elastic stiffening until reaching the maximum G'_t (2 to 3). During the subsequent strain reversal (3 to 4), the accumulated elastic energy dissipates viscously, indicating disruption of the internal microstructure. This process continues until a purely viscous regime is reached (negative G'_t). A negative G'_t signifies that stress decreases with increasing strain, reflecting a shift from elastic storage to complete viscous dissipation.[52,53,83] This indicates complete yielding and flow behaviour by point 4. Finally, as the strain returns to zero, viscous dissipation reduces, and the elastic modulus gradually recovers, closing the loop at point 1.

Overall, the intracycle analysis reveals that M300-stabilised PEs experience yielding through disruption and deformation of the close-packed droplet cages. In contrast, M800-stabilised PEs exhibit a more complex yielding process due to the presence of droplet clusters. These clusters introduce greater heterogeneity within the sample, leading to progressive deformation, stretching, and flow of the initial microstructure as the strain amplitude increases. These results reveal a clear difference in the microstructure of the two types of PEs, which is crucial for optimizing their application in transdermal drug delivery. For instance, M800-stabilised PEs, characterised by more complex droplet clusters, might exhibit a slower and potentially controlled release profile. The following section delves into the transdermal drug delivery properties of these PEs, exploring how the observed microstructural variations translate to drug release kinetics.

3.5 Transdermal release properties

The release profiles of all the investigated PEs are evaluated at room temperature and at physiological temperature (37 °C) using the procedure described in Section 2.4. Fig. 9A presents representative curves for the normalised cumulative release of samples M300-C1/C3 and M800-C1/C3 at room temperature.
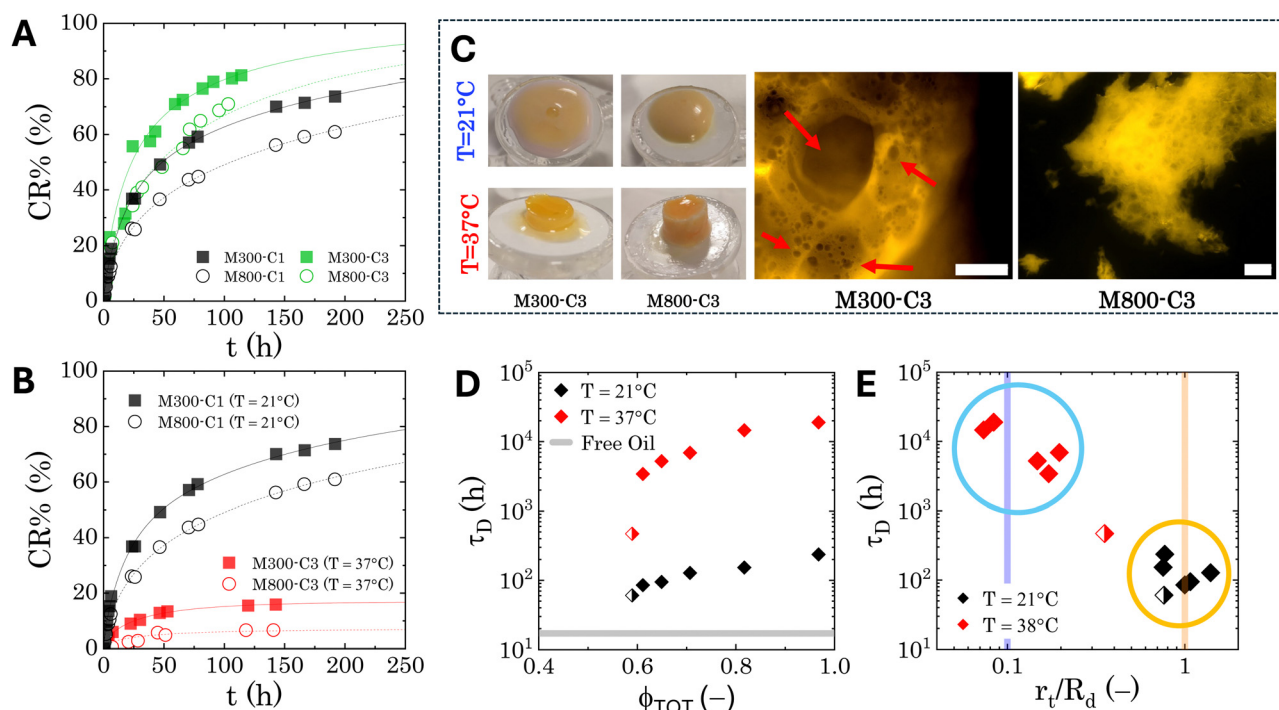

Fig. 9 Transdermal drug release model: results. (A) Normalised cumulative drug release at room temperature for M300- and M800-stabilized PEs containing different loadings of microgels. (B) Normalised cumulative drug release for samples M300-C1 and M800-C1 at both room temperature and physiological temperature. In both panels, the lines represent the fitting of the data to eqn (7). (C) Left: General appearance of the PEs after the release tests (approximately 190 hours) at room temperature (top row) and physiological temperature (bottom row). Right: Details of the microstructure of the samples treated at physiological temperature, obtained through fluorescence microscopy. The scale bars indicate 250 μm. The red arrows indicates some of the round voids left by droplets. (D) Characteristic diffusion time as a function of the total dispersed phase volume fraction (ϕ_{TOT}). The grey line reports the reference value for simple jojoba oil. (E) Characteristic diffusion time as a function of the normalised characteristic dimension of the traps obtained from fitting of eqn (7). The two vertical lines indicate the order of magnitude of the droplet size (yellow line) and the microgel size (blue line). Half-filled symbols in panels (D) and (E) indicate the formulation with $\phi_{TOT} < 0.6$.

This comparison emphasises the impact of microgel loading on the release profiles. Fig. 9B focuses on the thermoresponsive behaviour by depicting the normalised cumulative release of samples M300-C1 and M800-C1 at both room and physiological temperatures. All samples exhibit a cumulative release trend characteristic of diffusion-controlled kinetics.[2,84] This is typically characterised by an initial, steeper rise in concentration followed by a plateau as time approaches infinity. The release profiles clearly demonstrate the influence of both microgel loading and temperature. Interestingly, the bulk rheological properties do not appear to directly govern the release kinetics. This is evident from the slower release observed for sample M300-C1 compared to M800-C3 (Fig. 9A), despite M300-C1 having a lower storage modulus and yield stress (by 1 and 2 orders of magnitude, respectively). Conversely, a higher microgel loading appears to slow down the release kinetics, suggesting that the presence of microgels within the PEs structure contributes to the controlled release mechanism. Another intriguing observation is the significant decrease in release rate at higher temperatures for all samples. This might seem counter intuitive, as temperatures exceeding the microgel volume phase transition temperature (VPTT) are typically expected to induce phase separation in PEs due to the collapsed state of the microgels, thus causing release of the species from the single droplets acting as drug carriers.[42,85] However, the appearance of the PEs in the donor chamber after the release experiment is strikingly different for samples stored at physiological temperature (Fig. 9C). While room temperature samples retain their original consistency with some creaming, those exposed to 37 °C appear as textured cylindrical structures. To further investigate their internal structure, we sectioned a portion of these samples for observation under fluorescence microscopy. The results for reference samples M300-C3 and M800-C3 are shown in Fig. 9C. Bright areas represent the microgels, which are fluorescently labelled. As observed, microgels in both cases collapse, inducing significant clustering that immobilises the emulsions within a porous medium characterised by varying void sizes. M300-stabilized samples exhibit sparse round voids, left by oil droplets (as indicated by the arrows in Fig. 9C), while the dense microgel structures within the droplet clusters of M800-stabilised samples make it more challenging to distinguish individual voids.

To gain a deeper understanding of the relationship between microstructure and release kinetics, and to obtain more quantitative results, we employ a semi-empirical model to analyse all the release profiles. Considering the microstructural features of both fresh and temperature-treated samples, along with the geometry of the Franz cell, we model the drug transport as a two-step diffusive process: (i) transport within the PEs and (ii) transport across the polysulfone membrane of the Franz cell. For the first diffusion mechanism, we utilize a model for species transport within a porous medium containing randomly distributed traps.[86] This model predicts the following decay of concentration from the donor compartment:

$$\bar{c}(t) \sim \exp\left[-(t/\tau_{\mathrm{D}})^{d/(d+2)}\right] \quad (5)$$

Here $\bar{c}(t)$ represents the remaining drug concentration at time t. τ_{D} is the characteristic diffusion time between traps, defined as $\tau_{\mathrm{D}} = r_t^{-2}\mathcal{D}_t$, where r_t represents the characteristic size of the traps, and $\mathcal{D}_t$ is the diffusion coefficient. Finally, d is the spatial dimension, which equals 3 for a 3D system, resulting in a total exponent of 0.6. The characteristics of the second diffusion mechanism are determined using a control experiment with pure jojoba oil. The release profile follows a first-order diffusion decay (see SI-3 in the ESI†) described by the following equation:

$$\bar{c}(t) \sim \exp[-(t/\tau_0)] \quad (6)$$

where τ_0 is the characteristic diffusion time across the membrane, equal to 17.03 hours. Hence, by combining both eqn (5) and (6), the concentration of drug released from the PEs can be modelled as follows:

$$\bar{c}(t) = k\exp\left[-(t/\tau_{\mathrm{D}})^{0.6}\right] + (1-k)\exp(-t/\tau_0) \quad (7)$$

Here $0 < k < 1$ is a partition constant, which indicates the dominance of each mechanism.

Table 1 summarises the fitting results for all investigated PEs. Because the presence of microgels in the continuous phase significantly alters the PEs microstructure at physiological temperature, we also report the total dispersed phase volume fraction, ϕ_{TOT}. This value is calculated as the sum of the effective volume fraction, ϕ_{EFF}, and the residual microgel volume fraction within the continuous phase, ϕ_{m}. Details regarding the calculations of these volume fractions can be found in the ESI,† S5. For all Pickering emulsions, the partition constant consistently exceeds 0.7, indicating that the first diffusion mechanism within the PEs remains the dominant factor controlling release kinetics under all tested conditions. Notably, M800-stabilised samples exhibit significantly higher partition constant values, with most exceeding 0.9. This could be attributed to a higher degree of interconnection between droplets within M800-stabilised PEs and a lower residual microgel content in the continuous phase. This combination results in a more interconnected porous structure, where the porosity is primarily dictated by the distribution of droplets.

Table 1 Fitting parameters of the drug release model, τ_{D} and k, for all PEs investigated. The table also reports the total volume fraction of the dispersed phase, ϕ_{TOT}, calculated as specified in ESI S5

	Sample	ϕ_{TOT}	τ_{D} (h)	k
$T = 21\ °C$	M300-C1	0.817	152.9	0.808
	M300-C2	0.707	127.54	0.851
	M300-C3	0.59	60.45	0.783
	M800-C1	0.967	236.5	0.925
	M800-C2	0.65	94.5	0.953
	M800-C3	0.611	84.96	1
$T = 37\ °C$	M300-C1	0.817	$1.46 \times 10^{+4}$	0.894
	M300-C2	0.707	$6.88 \times 10^{+2}$	0.8
	M300-C3	0.59	$4.70 \times 10^{+2}$	0.707
	M800-C1	0.967	$1.9 \times 10^{+4}$	0.981
	M800-C2	0.65	$5.21 \times 10^{+3}$	0.917
	M800-C3	0.611	$3.41 \times 10^{+3}$	0.854

Interestingly, when plotting the characteristic diffusion times against the total volume fraction ϕ_{TOT}, we observe two distinct trends for each temperature, as shown in Fig. 9D. In both cases, the characteristic release time exhibits a strong positive correlation with the total volume fraction, showing an initial jump at a threshold value around 0.6, which is close to random packing conditions. At physiological temperature, when the microgels deswell, the entire curve shifts upwards by two orders of magnitude. This shift indicates a significant change in the characteristic size of the porosity of the material. To further investigate this, Fig. 9E plots the characteristic times against the characteristic size of the traps, normalised by the average radius of the droplets for each formulation. This visualisation reveals a transition in the dominant trap size. At room temperature, the characteristic size falls within the same order of magnitude as the droplet size. However, at physiological temperature, the characteristic size becomes comparable to the size of the microgels. The shift observed might be related to an increase in polymer density at the oil–water interface upon heating, caused by the hydrophobic collapse of the microgel network.[87] Additionally, the change in hydrophobicity can alter the interactions of the drug with the polymeric chains of the microgels, thus slowing down the release. Further investigations to properly characterise the mechanism at hand are surely required, however the present results highlight the crucial role of the local microstructure of the PEs in regulating sustained drug release.

4 Conclusions

In this study, we investigate how microgel size and thermo-responsive behaviour specifically influence the microstructure and rheology of Pickering emulsions to aid the design of transdermal drug delivery systems. To this end, we use model PEs stabilised with pNIPAM-based microgels of two distinct sizes (M300 and M800). PNIPAM microgels were chosen due to their well-established thermal responsiveness, allowing us to control their swelling behaviour using temperature as an external stimulus. The size of the resulting droplets was analysed using bright-field microscopy, while confocal microscopy revealed the arrangement of microgels at the droplet interface. Rheological properties were characterised using strain amplitude oscillatory sweep measurements and time-resolved analysis. Finally, the sustained release of levosimendan, a model lipophilic drug, was evaluated *via* the Franz-cell method at both room and physiological temperatures.

The microscopic analysis confirms that microgel size significantly affects microgel arrangement and interfacial coverage, ultimately impacting the PEs' rheological behaviour. Smaller M300 microgels form a more uniform and densely packed layer around the droplets, leading to less aggregation compared to PEs stabilised with larger M800 microgels. This difference in interfacial organisation translates to distinct rheological behaviours of the different formulations. More dispersed droplets with minimal inter-droplet connections exhibit a more fluid-like behaviour, while the presence of droplet clusters in the larger-microgel PEs introduces a more complex yielding process. The analysis of the intracycle nonlinear stress response suggests that M300-stabilised PEs yield through disruption and deformation of the close-packed droplet cages. In contrast, M800-stabilised PEs exhibit a more complex process due to rearrangements within the droplet clusters. These microstructural differences have a significant impact on the sustained drug release performance. For both PE types, the internal microstructure of the emulsions dominates the release kinetics. Notably, the characteristic release times directly correlate with the total volume fraction of the dispersed phases. The release mechanism can be modelled by considering the emulsion as a porous medium with randomly distributed traps. At room temperature, when the emulsions maintain their original structure, the characteristic size of these traps approximates the average droplet sizes. However, at physiological temperature, when the microgels significantly deswell, the characteristic release time increases significantly for both sets of PEs. Additionally, the dominant trap size shifts towards the microgel size. These findings highlight that microgel porosity also plays a crucial role in the sustained release of molecules from the PEs. It should be pointed out that, given the complex phase-change that the PEs undergo at physiological temperature, transient drug/MG interactions could also affect the release kinetics. Future studies should explore this aspect in more detail.

Overall, this study provides valuable insights into the relationship between microgel properties, microstructure, and the performance of PEs for drug delivery applications. In contrast to other drug delivery methods, such as hydrogel-based systems, where rheology and porosity are intrinsically linked, our study shows that PEs offer greater flexibility in decoupling rheological design from delivery properties. This decoupling allows for a wider range of formulation possibilities. Further investigations are required to explore the long-term stability and bio-compatibility of these PEs for *in vivo* applications, as well as the effect of shear flow on the release kinetics, relevant to the direct use of these formulation. Additionally, optimising the microgel design to achieve a balance between microstructure and desired release kinetics is an important area for future research.

Author contributions

Conceptualisation: SM, YL, PA, MP; data curation: SM, YL; formal analysis: SM; funding acquisition: YL, PA, SM; investigation: SM, YH; methodology: SM, YH; project administration: YL, PA, SM; resources: YL, PA, MP; supervision: YL, PA; visualization: SM; writing/original draft: SM; writing/review and editing: YL, PA, MP.

Data availability

All the data supporting this article have been included as part of the ESI.†

Conflicts of interest

There are no conflicts to declare.

Acknowledgements

Notes and references

1 J. Li and D. J. Mooney, *Nat. Rev. Mater.*, 2016, **1**, 1–17.

2 S. Hiranphinyophat, A. Otaka, Y. Asaumi, S. Fujii and Y. Iwasaki, *Colloids Surf., B*, 2021, **197**, 111423.

3 K. Wood, M. R. Szewczuk, D. Rousseau and R. J. Neufeld, *Oncotarget*, 2018, **9**, 12754–12768.

4 C. Pacheco, A. Baião, T. Ding, W. Cui and B. Sarmento, *Adv. Drug Delivery Rev.*, 2023, **194**, 114724.

5 W. Y. Jeong, M. Kwon, H. E. Choi and K. S. Kim, *Biomater. Res.*, 2021, **25**, 24.

6 M. I. Khan, M. I. Hossain, M. K. Hossain, M. H. K. Rubel, K. M. Hossain, A. M. U. B. Mahfuz and M. I. Anik, *ACS Appl. Bio Mater.*, 2022, **5**, 971–1012.

7 J. Marto, A. Ascenso, S. Simoes, A. J. Almeida and H. M. Ribeiro, *Expert Opin. Drug Delivery*, 2016, **13**, 1093–1107.

8 S. Peito, D. Peixoto, I. Ferreira-Faria, A. Margarida Martins, H. Margarida Ribeiro, F. Veiga, J. Marto and A. Cláudia Paiva-Santos, *Int. J. Pharm.*, 2022, **615**, 121455.

9 F. Sabbagh and B. S. Kim, *J. Controlled Release*, 2022, **341**, 132–146.

10 V. Phatale, K. K. Vaiphei, S. Jha, D. Patil, M. Agrawal and A. Alexander, *J. Controlled Release*, 2022, **351**, 361–380.

11 S. Chaturvedi and A. Garg, *J. Drug Delivery Sci. Technol.*, 2021, **62**, 102355.

12 A. Sharkawy, F. M. Casimiro, M. F. Barreiro and A. E. Rodrigues, *Int. J. Biol. Macromol.*, 2020, **147**, 150–159.

13 F. B. de Carvalho-Guimarães, K. L. Correa, T. P. de Souza, J. R. Rodríguez Amado, R. M. Ribeiro-Costa and J. O. C. Silva-Júnior, *Pharmaceuticals*, 2022, **15**, 1413.

14 R. Valjakka-Koskela, J. Hirvonen, J. Mönkkönen, J. Kiesvaara, S. Antila, L. Lehtonen and A. Urtti, *Eur. J. Pharm. Sci.*, 2000, **11**, 343–350.

15 R. S. Riley, C. H. June, R. Langer and M. J. Mitchell, *Nat. Rev. Drug Discovery*, 2019, **18**, 175–196.

16 G. Agrawal and R. Agrawal, *Polymers*, 2018, **10**, 418.

17 B. Wu, Y. Li, Y. Li, H. Li, S. Ji and Q. Xia, *React. Funct. Polym.*, 2021, **169**, 105074.

18 B. Pang, H. Liu and K. Zhang, *Adv. Colloid Interface Sci.*, 2021, **296**, 102522.

19 T. Zhang, F. Liu, J. Wu and T. Ngai, *Particuology*, 2022, **64**, 110–120.

20 H. Jiang, Y. Sheng and T. Ngai, *Curr. Opin. Colloid Interface Sci.*, 2020, **49**, 1–15.

21 F. A. Plamper and W. Richtering, *Acc. Chem. Res.*, 2017, **50**, 131–140.

22 M. Rey, M. A. Fernandez-Rodriguez, M. Karg, L. Isa and N. Vogel, *Acc. Chem. Res.*, 2020, **53**, 414–424.

23 M. A. Fernandez-Rodriguez, A. Martín-Molina and J. Maldonado-Valderrama, *Adv. Colloid Interface Sci.*, 2021, **288**, 102350.

24 F. Pinaud, K. Geisel, P. Massé, B. Catargi, L. Isa, W. Richtering, V. Ravaine and V. Schmitt, *Soft Matter*, 2014, **10**, 6963–6974.

25 S. Migliozzi, Y. He, P. Angeli and Y. Lan, *Colloids Surf., A*, 2024, 134538.

26 M. Destribats, V. Lapeyre, M. Wolfs, E. Sellier, F. Leal-Calderon, V. Ravaine and V. Schmitt, *Soft Matter*, 2011, **7**, 7689–7698.

27 M. Destribats, M. Eyharts, V. Lapeyre, E. Sellier, I. Varga, V. Ravaine and V. Schmitt, *Langmuir*, 2014, **30**, 1768–1777.

28 M. M. Schmidt, S. Bochenek, A. A. Gavrilov, I. I. Potemkin and W. Richtering, *Langmuir*, 2020, **36**, 11079–11093.

29 S. Aben, C. Holtze, T. Tadros and P. Schurtenberger, *Langmuir*, 2012, **28**, 7967–7975.

30 T. G. Mason, J. Bibette and D. A. Weitz, *Phys. Rev. Lett.*, 1995, **75**, 2051–2054.

31 B. P. Binks, J. H. Clint and C. P. Whitby, *Langmuir*, 2005, **21**, 5307–5316.

32 S. S. Datta, D. D. Gerrard, T. S. Rhodes, T. G. Mason and D. A. Weitz, *Phys. Rev. E: Stat., Nonlinear, Soft Matter Phys.*, 2011, **84**, 041404.

33 M. Kaganyuk and A. Mohraz, *J. Colloid Interface Sci.*, 2019, **540**, 197–206.

34 J. S. Hong, H. J. Kong, K. Hyun, J. Bergfreund, P. Fischer and K. H. Ahn, *Rheol. Acta*, 2019, **58**, 453–466.

35 J. Hou, H.-N. Xu, L. Wang and L. Zhang, *Langmuir*, 2022, **38**, 4599–4605.

36 P. L. Fuhrmann, S. Breunig, G. Sala, L. Sagis, M. Stieger and E. Scholten, *J. Colloid Interface Sci.*, 2022, **607**, 389–400.

37 W. Jin, J. Zhu, Y. Jiang, P. Shao, B. Li and Q. Huang, *J. Agric. Food Chem.*, 2017, **65**, 1401–1409.

38 Y. Chen, W. Wei, Y. Zhu, J. Luo, R. Liu and X. Liu, *ACS Appl. Mater. Interfaces*, 2020, **12**, 4821–4832.

39 Y. Ming, Y. Xia and G. Ma, *Aggregate*, 2022, **3**, e162.

40 L. Dai, Y. Li, F. Kong, K. Liu, C. Si and Y. Ni, *ACS Sustainable Chem. Eng.*, 2019, **7**, 13497–13504.

41 M.-h Kwok, J. Ambreen and T. Ngai, *J. Colloid Interface Sci.*, 2019, **546**, 293–302.

42 T. Ngai, S. H. Behrens and H. Auweter, *Chem. Commun.*, 2005, 331–333.

43 X. Wang, X. Qiu and C. Wu, *Macromolecules*, 1998, **31**, 2972–2976.

44 R. Neupane, S. H. Boddu, J. Renukuntla, R. J. Babu and A. K. Tiwari, *Pharmaceutics*, 2020, **12**(2), 152.

45 F. Iliopoulos, P. J. Caspers, G. J. Puppels and M. E. Lane, *Pharmaceutics*, 2020, **12**(9), 887.

46 X. Wu, R. Pelton, A. Hamielec, D. Woods and W. McPhee, *Colloid Polym. Sci.*, 1994, **272**, 467–477.

47 J. Liu, C. S. Y. Tan, Z. Yu, N. Li, C. Abell and O. A. Scherman, *Adv. Mater.*, 2017, **29**, 1605325.

48 S. Arditty, C. Whitby, B. Binks, V. Schmitt and F. Leal-Calderon, *Eur. Phys. J. E: Soft Matter Biol. Phys.*, 2003, **11**, 273–281.

49 S. A. Rogers, *J. Rheol.*, 2012, **56**, 1129–1151.

50 S. A. Rogers and M. P. Lettinga, *J. Rheol.*, 2012, **56**, 1–25.

51 S. A. Rogers, *Rheol. Acta*, 2017, **56**, 501–525.

52 J. Choi, F. Nettesheim and S. A. Rogers, *Phys. Fluids*, 2019, **31**, 073107.

53 G. J. Donley, J. R. de Bruyn, G. H. McKinley and S. A. Rogers, *J. Non-Newtonian Fluid Mech.*, 2019, **264**, 117–134.

54 S. Migliozzi, P. Angeli and L. Mazzei, *Materials*, 2021, **14**, 1782.

55 J. Xu, P. Wang, Z. Zhou, B. Yuan and H. Zhang, *J. Rheol.*, 2024, **68**, 491–508.

56 M. Wilhelm, D. Maring and H. W. Spiess, *Rheol. Acta*, 1998, **37**, 399–405.

57 R. H. Ewoldt, A. E. Hosoi and G. H. McKinley, *J. Rheol.*, 2008, **52**, 1427–1458.

58 G. Del Monte, D. Truzzolillo, F. Camerin, A. Ninarello, E. Chauveau, L. Tavagnacco, N. Gnan, L. Rovigatti, S. Sennato and E. Zaccarelli, *Proc. Natl. Acad. Sci. U. S. A.*, 2021, **118**, e2109560118.

59 E. Ponomareva, B. Tadgell, M. Hildebrandt, M. Krüsmann, S. Prévost, P. Mulvaney and M. Karg, *Soft Matter*, 2022, **18**, 807–825.

60 R. Acciaro, T. Gilanyi and I. Varga, *Langmuir*, 2011, **27**, 7917–7925.

61 R. Pelton, H. Pelton, A. Morphesis and R. Rowell, *Langmuir*, 1989, **5**, 816–818.

62 D. Vlassopoulos and M. Cloitre, *Curr. Opin. Colloid Interface Sci.*, 2014, **19**, 561–574.

63 S. Migliozzi, G. Meridiano, P. Angeli and L. Mazzei, *Soft Matter*, 2020, **16**, 9799–9815.

64 M. Mooney, *J. Colloid Sci.*, 1951, **6**, 162–170.

65 V. Schmitt and V. Ravaine, *Curr. Opin. Colloid Interface Sci.*, 2013, **18**, 532–541.

66 M.-C. Tatry, E. Laurichesse, J. Vermant, V. Ravaine and V. Schmitt, *J. Colloid Interface Sci.*, 2023, **629**, 288–299.

67 E. L. Hinrichsen, J. Feder and T. Jøssang, *Phys. Rev. A: At., Mol., Opt. Phys.*, 1990, **41**, 4199–4209.

68 H. Zhao, Y. Yang, Y. Chen, J. Li, L. Wang and C. Li, *Chem. Eng. Sci.*, 2022, **248**, 117085.

69 M. Destribats, V. Lapeyre, E. Sellier, F. Leal-Calderon, V. Ravaine and V. Schmitt, *Langmuir*, 2012, **28**, 3744–3755.

70 N. Koumakis, A. Pamvouxoglou, A. S. Poulos and G. Petekidis, *Soft Matter*, 2012, **8**, 4271–4284.

71 B. C. Munro, S. B. Hall and C. P. Whitby, *Colloids Surf., A*, 2022, **637**, 128237.

72 K. Hyun, S. H. Kim, K. H. Ahn and S. J. Lee, *J. Non-Newtonian Fluid Mech.*, 2002, **107**, 51–65.

73 D. Bonn, M. M. Denn, L. Berthier, T. Divoux and S. Manneville, *Rev. Mod. Phys.*, 2017, **89**, 035005.

74 A. Ghosh, G. Chaudhary, J. G. Kang, P. V. Braun, R. H. Ewoldt and K. S. Schweizer, *Soft Matter*, 2019, **15**, 1038–1052.

75 M. Cloitre, R. Borrega, F. Monti and L. Leibler, *Phys. Rev. Lett.*, 2003, **90**, 068303.

76 J. Seth, L. Mohan, C. Locatelli-Champagne, M. Cloitre and R. T. Bonnecaze, *Nat. Mater.*, 2011, **10**, 838–843.

77 C. P. Whitby and M. Krebsz, *Soft Matter*, 2014, **10**, 4848–4854.

78 N. Koumakis and G. Petekidis, *Soft Matter*, 2011, **7**, 2456–2470.

79 K. N. Pham, G. Petekidis, D. Vlassopoulos, S. U. Egelhaaf, W. C. K. Poon and P. N. Pusey, *J. Rheol.*, 2008, **52**, 649–676.

80 C. Pellet and M. Cloitre, *Soft Matter*, 2016, **12**, 3710–3720.

81 R. H. Ewoldt, P. Winter, J. Maxey and G. H. McKinley, *Rheol. Acta*, 2010, **49**, 191–212.

82 S. Wojno, A. Ahlinder, A. Altskär, M. Stading, T. Abitbol and R. Kádár, *Carbohydr. Polym.*, 2023, **308**, 120622.

83 J. D. Park and S. A. Rogers, *Phys. Fluids*, 2020, **32**, 063102.

84 J. Siepmann, F. Lecomte and R. Bodmeier, *J. Controlled Release*, 1999, **60**, 379–389.

85 Z. Li, W. Richtering and T. Ngai, *Soft Matter*, 2014, **10**, 6182–6191.

86 D. Tartakovsky and M. Dentz, *Transp. Porous Med.*, 2019, **130**, 105–127.

87 D. Kleinschmidt, K. Nothdurft, M. V. Anakhov, A. A. Meyer, M. Mork, R. A. Gumerov, I. I. Potemkin, W. Richtering and A. Pich, *Mater. Adv.*, 2020, **1**, 2983–2993.